Research

Check for updates

Author for correspondence:
A. Kao
e-mail: a.kao@gre.ac.uk

Thermoelectric magnetohydrodynamic control of melt pool dynamics and microstructure evolution in additive manufacturing

A. Kao[1], T. Gan[1], C. Tonry[1], I. Krastins[1,2] and K. Pericleous[1]

[1]Centre for Numerical Modelling and Process Analysis, University of Greenwich, Old Royal Naval College, Park Row, London SE109LS, UK
[2]Institute of Physics, University of Latvia, 32 Miera iela, Salaspils 2169, Latvia

AK, 0000-0002-6430-2134

Large thermal gradients in the melt pool from rapid heating followed by rapid cooling in metal additive manufacturing generate large thermoelectric currents. Applying an external magnetic field to the process introduces fluid flow through thermoelectric magnetohydrodynamics. Convective transport of heat and mass can then modify the melt pool dynamics and alter microstructural evolution. As a novel technique, this shows great promise in controlling the process to improve quality and mitigate defect formation. However, there is very little knowledge within the scientific community on the fundamental principles of this physical phenomenon to support practical implementation. To address this multiphysics problem that couples the key phenomena of melting/solidification, electromagnetism, hydrodynamics, heat and mass transport, the lattice Boltzmann method for fluid dynamics was combined with a purpose-built code addressing solidification modelling and electromagnetics. The theoretical study presented here investigates the hydrodynamic mechanisms introduced by the magnetic field. The resulting steady-state solutions of modified melt pool shapes and thermal fields are then used to predict the microstructure evolution using a cellular automata-based grain growth model. The results clearly demonstrate that the hydrodynamic mechanisms

THE ROYAL SOCIETY
PUBLISHING

and, therefore, microstructure characteristics are strongly dependent on magnetic field orientation.

This article is part of the theme issue 'Patterns in soft and biological matters'.

1. Introduction

Additive manufacturing (AM) is the process of joining materials together, typically in a layer-by-layer approach to construct three-dimensional objects. In the case of AM processing in metals, a high energy source, typically a laser or electron beam, is used to melt metallic powder layers successively onto each other, allowing layers to join as they solidify. There are several AM processes employed by industry for metal component production. Two widely used examples include selective laser melting (SLM), where a thin layer of powder is spread across the print bed, proceeding from a CAD file, specific regions are melted, a new layer of powder is spread across the top and the process repeats [1–5]. In the alternative direct energy deposition (DED) technique, the powder is continuously deposited and melted by the laser [6,7]. Both of these processes generate a liquid melt pool that travels in the direction of the energy source and solidifies in its wake. From the modelling point of view, laser AM for metals is essentially a fast-rate welding process and as such a host to a plethora of complex physical phenomena. In the melt pool, one needs to consider heat transfer and phase change in what is an inhomogeneous particle bed medium, heat loss by radiation [8], evaporative heat and mass loss [9], Marangoni flow driven by surface tension changes [10], spattering [11], denudation [12], etc. As the pool solidifies, the microstructure develops and then it is modified or possibly remelted as the laser scan is repeated on further powder layer deposition. The repeated melting/solidification of layers, the inhomogeneous properties of the bed and the presence of interstitial gas lead to a number of defects that affect the integrity of components. This paper provides a precursor for novel techniques to eliminate some of these defects.

Numerical models of this process range across a wide range of length scales from the macroscale that investigates the entire build geometry [13], to mesoscopic scales that focus on melt pool dynamics [11,14] and to microscopic scales that capture the microstructure [15,16]. On the mesoscopic scale, as there is a direct analogy to welding, methods are typically focused around conservation of energy and directly address the thermal problem [17]; however, in the context of AM, models now also need to account for melting powders and other physical phenomena [11,18]. On the microstructure side, there are two frequently used methods, first the phase field method [15,16] can capture the dendritic scale but requires a very fine computational mesh and so only small sections can be modelled. The second is the cellular automata method (CA), which is generally used to predict the grain scale and can capture larger sections of the build [19–21].

From the industrial point of view, AM is an attractive process allowing for the production of complex geometries that may otherwise be impossible to create using traditional techniques or may require extensive subtractive manufacturing with time cost and the loss of material. The use of AM is becoming widespread with diverse applications ranging from energy [22] to biomedical implants [23] to the fabrication of aero-engine parts [24]. However, the process can also introduce defects [25] that are detrimental to the structural integrity of the final components, including the formation of pores [26], cracks [27] and large columnar grains through epitaxial growth [4]. Large variations in alloy composition lead to variations in structural properties, where, for example, the melt pool boundaries act as sites for failure [4]. Many of these defects can be associated with the contrasting solidification conditions encountered compared to traditional casting techniques, where in AM, as in welding, there are both large thermal gradients and rapid cooling. Therefore, additional control mechanisms are actively being sought that can both manipulate the melt pool and subsequently the microstructure in a positive way. One relatively unexplored technique is that of the application of an external magnetic field to exploit the thermoelectric magnetohydrodynamic (TEMHD) phenomenon.

Thermoelectric (TE) currents are a natural and inherent part of many solidification processes and are generated by thermal gradients and variations in the Seebeck coefficient. In the presence of an applied magnetic field, the TE currents interact generating a Lorentz force that drives flow, convectively transporting both heat and mass. Significant changes to solidification processes due to TEMHD have been observed experimentally and predicted theoretically in situations ranging from the low thermal gradient and slow solidification typical of directional solidification processes [28–30] to the high thermal and rapid solidification process of high undercooled growth [31,32]. In terms of solidification conditions, AM thermal gradients are high with moderate solidification velocities compared to high undercooled growth, and, therefore, TEMHD effects could be quite significant. To the authors' knowledge, there is a lack of scientific investigations into the effects of TEMHD in AM; only recently has the first experimental paper appeared [33] showing that the application of a 0.12 T magnetic field leads to beneficial effects, such as a decrease in pore density and reduced columnar grain morphology. To date, no theoretical or computational modelling has been conducted to predict, describe or explain these observations. Referring to the closely related field of welding, there have been more investigations. Chen *et al*. [34] conducted welding experiments using 304 Stainless steel and a 0.415 T static axial magnetic field, where they showed a reduction in width within the transitional region in the microstructure. Elsewhere, Kern *et al*. [35] showed that by applying a 0.3 T transverse magnetic field, the 'humping' welding defect, which is analogous to 'balling' in AM that leads to beading, could be suppressed and they concluded that this effect could be attributed to TE forces.

These sparse investigations have demonstrated that the application of a magnetic field can have a transformative effect on both the melt pool and microstructure, yet there has been no methodical study to understand the link between these changes and TEMHD fluid flow. This paper aims to reveal the fundamental hydrodynamic mechanisms of TEMHD and the potential effect it has on the microstructure of AM and related processes.

2. Methodology

To model the influence of TEMHD in the AM process, a fully coupled approach is taken to capture the mesoscopic melt pool dynamics, the steady-state solutions of which are then used to predict microstructure evolution. In this work, the system represents an Al10Si alloy. This section describes the governing set of equations for each of the physical phenomena present, and the numerical methods used to solve them.

TE currents, $\mathbf{J}$, are calculated from a modified Ohm's Law [36] given by

$$\mathbf{J} = \sigma(\mathbf{E} + \mathbf{u} \times \mathbf{B} - S\nabla T), \tag{2.1}$$

where σ is the electrical conductivity, $\mathbf{E}$ is the electric field, $\mathbf{u}$ is the fluid velocity, $\mathbf{B}$ is the magnetic flux density, S is the Seebeck coefficient and T is the temperature. The electric potential ψ is related to $\mathbf{E}$ by $\mathbf{E} = -\nabla\psi$. Conservation of charge dictates that $\nabla \cdot \mathbf{J} = 0$ and so the conservative $\mathbf{E}$ field reacts to the non-conservative TE field, $S\nabla T$, to preserve this condition. The term $\mathbf{u} \times \mathbf{B}$ is the induced field and ultimately responsible for electromagnetic damping of fluid flow. The resulting current interacts with the magnetic field to generate a Lorentz force, $\mathbf{F} = \mathbf{J} \times \mathbf{B}$. In the liquid, this force drives fluid motion governed by the Navier–Stokes equation

$$\rho\left(\frac{\partial \mathbf{u}}{\partial t} + \mathbf{u} \cdot \nabla\mathbf{u}\right) = -\nabla p + \mu\nabla^2\mathbf{u} + \mathbf{J} \times \mathbf{B}, \tag{2.2}$$

where t is time, ρ is the density, p is pressure and μ is the dynamic viscosity. Conservation of mass for incompressible fluid flow provides the condition $\nabla \cdot \mathbf{u} = 0$. Fluid flow then introduces convective heat transport governed by

$$\frac{\partial T}{\partial t} = \nabla \cdot \alpha\nabla T - \mathbf{u} \cdot \nabla T, \tag{2.3}$$

where α is the thermal diffusivity. During solidification and melting, latent heat of fusion, L_f, is related to temperature through the volumetric enthalpy, H, which is defined as the sum of latent and sensible heats

$$H = fL_f + c_pT, \tag{2.4}$$

where c_p is the specific heat capacity and the phase variable f is the liquid fraction, with $f = 1$ representing fully liquid and $f = 0$ fully solid states. Intermediate values represent the transition between phases from either melting or solidification.

Equations (2.1)–(2.4) represent the physics of the problem and in the numerical procedure used, they are weakly coupled such that solutions for the unknown variables are calculated over a time interval $\Delta t = 0.1\,\mu s$ in each equation and then used successively in the next equation. For a given thermal field, equation (2.1) along with the conservation of charge gives Poisson's equation for the electric potential $\mathbf{J}$ and subsequently $\mathbf{J} \times \mathbf{B}$ can be calculated appearing as a source term in equation (2.2). The Navier–Stokes equations are solved using the lattice Boltzmann method (LBM) [37,38] yielding a solution for $\mathbf{u}$. Heat transport is then calculated from equation (2.3), and finally the change of phase and release of latent heat are calculated in equation (2.4). Solutions for the electric potential, thermal transport and the enthalpy method use finite difference-based schemes [29,39].

The computational domain is a cuboid divided into cubes of side $\Delta x = 5\,\mu m$. The top surface of the domain at $+\hat{z}$ represents the boundary between the atmosphere and the AM process. Equations (2.1)–(2.4) are solved throughout the entire computational domain; however, at the boundaries, especially the top surface, additional phenomena from the AM process are introduced. Variations in temperature lead to changes in surface tension γ and to the appearance of a surface Marangoni stress given by

$$F_M = \frac{\partial \gamma}{\partial T}\nabla T. \tag{2.5}$$

On the thermal side, the AM process introduces three key heat sources/sinks at the surface: the heating laser, latent heat loss due to evaporation and heat loss from radiation. The total heat flux at this surface [40,41] is given by

$$Q = \frac{3P}{\pi r_h^2}\exp\left(-3\left(\frac{r}{r_h}\right)^2\right) - H_v p_0 \exp\left(\frac{H_v}{R}\left(\frac{1}{T_v} - \frac{1}{T}\right)\right)\sqrt{\frac{m}{2\pi k_B T}} - \sigma_B \epsilon (T^4 - T_{ref}^4). \tag{2.6}$$

The first term is heat flux from the laser represented as a Gaussian distribution, where P is the effective laser power, r_h is the spot radius and r is the radius from the centre of the spot. The second term is evaporation where H_v is the evaporation enthalpy, p_0 is the atmospheric pressure, R is the ideal gas constant, T_v is the evaporation temperature, m is the mass of a single vapour particle (atomic weight) and k_B is the Boltzmann constant. The final term is the radiation loss, where σ_B is the Stefan–Boltzmann constant, ϵ is the emissivity and T_{ref} is the reference temperature. The other domain boundaries represent far-field conditions, namely the ambient temperature. For current density, the atmosphere is assumed to be non-conductive and the system is closed, hence no normal current appears on any of the boundaries.

The laser scans across the top surface in $+\hat{x}$ with a velocity, u_s, heating the top surface. As the powder melts a liquid pool forms and heat is transported through the system by diffusion and convection. Evaporative and radiative cooling occurs at the surface and heat is transported through the powder by conduction. As the laser moves and regions of the melt pool cool down, solidification occurs. In contrast with welding, these solidified regions can have very different material properties compared to the initial powder phase. Two key materials properties of interest here are the electrical conductivity and thermal diffusivity, where the powder phase diffusivity can be 5–10% lower than the solid [42]. A similar drop is taken for the electrical conductivity by assuming the Wiedemann–Franz law holds true. This law shows the electrical conductivity to be proportional to the thermal diffusivity. To account for this transition, a second discrete phase variable Ψ acts as a tag, initially set to powder, $\Psi = -1$, then, when a computational cell melts, it

becomes liquid, $\Psi = 0$, and when a cell solidifies, solid, $\Psi = 1$. Solid cells can remelt but cannot then come back as powder. Ψ is then used to assign corresponding material properties to each of the three phases.

To prevent far-field boundaries from influencing the solution as the laser moves, a moving mesh approach is adopted. The moving mesh moves at the same speed as the scanning laser, but in the opposite direction. This has the effect of keeping the laser spot in the same relative position in the domain allowing for a large enough time for the system to reach steady conditions and removing the need for a very large domain. From a practical perspective, information of all variables is passed to neighbouring cells, for example $f(x, y, z) = f(x + \Delta x, y, z)$. At the $-\hat{x}$ boundary information is lost, while at $+\hat{x}$ boundary, far-field conditions are introduced to the domain.

Microstructure evolution is predicted using a CA, which can capture the microstructure at the scale of the melt pool. The method used here is based on the μMatIC code [43–45] and recently applied by the authors to convection-based problems [28,29]. The mesoscopic steady-state solutions for temperature and velocity are used as inputs to the microstructure model, providing a one-way coupling from the meso- to micro-scale. The domain size of the microstructure model is identical to the mesoscopic model, but with a much smaller cell size, with $\Delta x = 1\,\mu m$. The temperature and velocity profiles from the mesoscopic solutions are interpolated onto this finer grid. The thermal field essentially controls the melt pool shape in the CA, while the velocity field feeds into the transport equations and affects the redistribution of solute across the melt pool. As the hydrodynamics and thermal problems are not recalculated, this reduces to solving the coupled transport and solidification equation set. Although the cell size is five times smaller a larger time step of $\Delta t = 1\,\mu s$ can be used as the highly nonlinear effects and their coupling such as radiation, evaporation, Marangoni and TEMHD flows are already resolved.

The CA also uses a continuous solid fraction phase variable ϕ_s to represent solidification. For alloy solidification, the concentration of solute in the solid, C_s, and liquid, C_l, are governed by $C_s = k_e C_l$, where $k_e = 0.13$ is the equilibrium partition coefficient of solute. Owing to the relatively rapid solidification of AM processes, the non-equilibrium effect of solute trapping is introduced. To account for this, the continuous growth model by Aziz & Kaplan [46] proposed a change to the partition coefficient given by

$$k = \frac{k_e + V/V_D}{1 + V/V_D},\qquad(2.7)$$

where V is the growth velocity and V_D is the 'diffusion' velocity. In this case, $V = u_s$ the scan velocity and $V_D \approx D_l/L$, where L is some characteristic length scale. At the interface, the solid fraction rate of change is given by

$$C_l(1-k)\frac{\partial \phi_s}{\partial t} = -\nabla \cdot (D_e \nabla C_l) + [1 - (1-k)\phi_s]\frac{\partial C_l}{\partial t},\qquad(2.8)$$

where $D_e = \phi_l D_l + \phi_s D_s$ is the equivalent diffusion coefficient. The equilibrium interface temperature, T^i, is calculated from the alloy phase diagram using $T^i = m_l(C_l - C_0)$, where m_l is the liquidus slope and C_0 is a reference concentration. Convective transport of solute is governed by

$$\frac{\partial C_e}{\partial t} + \mathbf{u} \cdot \nabla C_l = \nabla \cdot (D_e \nabla C_l),\qquad(2.9)$$

where the equivalent concentration is defined as $C_e = (1 - \phi_S)C_l + \phi_s C_s$. Even with this smaller cell size, the dendritic scale can still be even smaller than this in AM processes. The eutectic often forms at nanoscales [47] and so to accurately capture the microstructure a cell size less than 0.1 μm would be required. From a computational perspective, for the domain sizes used in this work up to a trillion cells would be required, which is unfeasible and extremely powerful high performance computing would be necessary. Therefore, to predict the redistribution of concentration, a volume-averaged approach is taken where a cell is considered to be filled with both low-concentration dendrites and high-concentration eutectic. From a physical perspective,
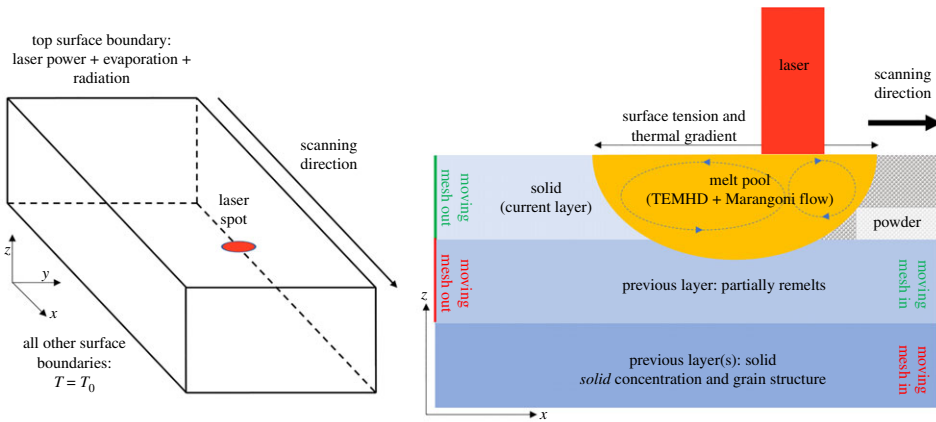
Figure 1. Schematic of the numerical model for AM processing.

the characteristic length, L, represents the interface thickness and for $k = 0.7$ used in this work, gives $L = 38$ nm, which is consistent with values used in phase field modelling that require an interface thickness as part of the formulation [15,16]. However, due to the disparate spatial scale between microstructure features and the cell size, liquid regions in the mushy zone where solute would be ejected cannot be resolved and are essentially considered solid or solidifying (and therefore are also ejecting solute) in the numerical model. Therefore, from a numerical perspective, an even higher partition coefficient may be more appropriate. For example, L could represent the inter-dendritic spacing of 0.1 µm, giving $k = 0.85$ or even the cell size of 1 µm, giving $k = 0.98$. However, with increasing partition coefficient, the system will behave more like a pure material with no ejected solute. Consequently, solute variations will become vanishing and so the ability to predict the microstructure.

The microstructure model is used to capture multiple layers of the AM process. A periodic approach is taken, where, as the solidified cells exit the back of the domain through the moving mesh, they are reintroduced to the front, but lowered by the powder layer depth and above this a new powder layer is introduced. In the results presented, 12 layers are captured. With only a one-way coupling, changes to the temperature from higher thermal diffusivity of previous solid layers are not accounted for nor is solute undercooling. However, the microstructure model does provide an indication of the grain structure and the relative distribution of solute in the final solid structure.

A schematic of the problem set-up is given in figure 1, highlighting the domain geometry, boundary conditions and key physics. Table 1 gives values of material properties representative of Al10Si and process parameters that are used in the numerical calculations. In calculating the effective laser power, an efficiency of 0.7 has been assumed, so for a 100 W laser, 70 W enters the system.

3. Results and discussion

Preliminary studies described in the introduction have shown that the magnetic field direction relative to scan direction can have a significant influence on pool dynamics and consequently microstructure [33,35]. A parametric study of the magnetic field orientation was conducted to understand the various TEMHD hydrodynamic mechanisms and the intimate coupling to the thermal transport and microstructure evolution. For the cases with an applied magnetic field, the strength is taken as $|\mathbf{B}| = 0.5$ T, with the exception of the investigation into the transition from Marangoni to TEMHD flow. For the cases presented, $|\mathbf{B}| = 0.5$ T was found to be sufficient for TEMHD to be the dominant force.

Table 1. Material properties of Al10Si and process parameters used in numerical simulations.

material properties	symbol	value	unit
specific heat capacity	c_p	1200 [48]	J kg^{-1} K
thermal diffusivity liquid	α_l	1×10^{-5} [49]	m^2 s^{-1}
thermal diffusivity solid	α_s	2×10^{-5} m^2 s^{-1} [49]	m^2 s^{-1}
thermal diffusivity powder	α_p	2×10^{-6} m^2 s^{-1}	m^2 s^{-1}
melting point	T_m	993.45 K	K
vaporization point	T_v	2743.15 K	K
emissivity	ϵ	0.17	—
heat of vaporization	H_v	1.05×10^7	J kg^{-1}
heat of fusion	H	3.96×10^5 [50]	J kg^{-1}
radiation reference temperature	T_{ref}	293	K
Seebeck power	ΔS	1×10^{-4} [51]	V K^{-1}
electrical conductivity liquid	σ_l	2×10^6	S m^{-1}
electrical conductivity solid	σ_s	1×10^7	S m^{-1}
electrical conductivity powder	σ_p	1×10^6	S m^{-1}
density	ρ	2380 [50]	kg m^{-3}
dynamic viscosity	μ	1.3×10^{-3}	Pa S
temperature dependence on surface tension	$\frac{\partial \gamma}{\partial T}$	-1.27×10^{-4} [50]	N m^{-1} K
mass diffusivity	D_l	2×10^{-9}	m^2 s^{-1}
partition coefficient (volume approximation)	k	0.7	—
liquidus slope	m_l	-8.2	K wt%$^{-1}$
parameters			
effective laser power (assuming 0.7 efficiency)	P	100 (70)	W
beam radius	r_h	100	μm
atmospheric pressure	p_0	101 325	Pa
scan speed	u_s	0.1	m s^{-1}
cell size enthalpy method	Δx	5	μm
cell size CA	Δx	1	μm
domain length	x	800	μm
domain width	y	600	μm
domain depth	z	300	μm

(a) Case 1: control case, $\hat{B} = 0$

This first case investigates the numerical model's behaviour in the absence of a magnetic field. In the vicinity of the laser spot, the temperature is high decreasing towards the edges of the melt pool. As the laser is moving, the temperature is transported upstream and both the isotherms and melt pool take on an oblate shape. Upstream is defined as the direction where the laser has already scanned and downstream is the direction the laser is scanning. Upstream the liquid solidifies and due to the disparity in thermal diffusivity between the solid (higher) and the powder (lower), more heat penetrates into the solid upstream further extending the thermal field. Strong thermal
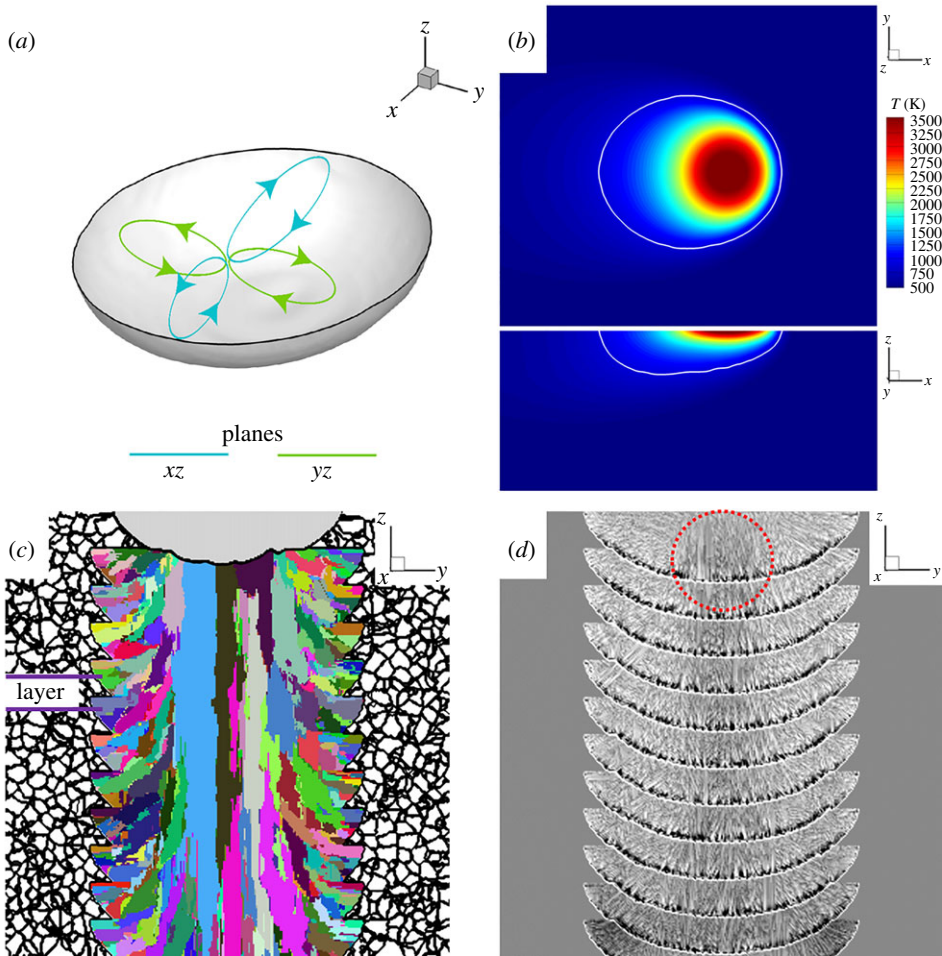
Figure 2. $\hat{\mathbf{B}} = 0$. (*a*) Hydrodynamic mechanism and (*b*) thermal field. Cross-section of microstructure perpendicular to scan direction (*c*) Grain structure with indication of the layer thickness (*d*) Concentration, the red circle highlighting the region of high concentration.

gradients of the order $\nabla T = 10^7 \mathrm{K\,m^{-1}}$ emanate radially from the laser spot introducing strong variations in surface tension that drive radial Marangoni flow from the laser spot axis along the top surface of the melt pool. Continuity of mass causes the fluid flow to circulate down to the bottom of the melt pool and then back up at the laser spot. Marangoni convection causes hot fluid to be transported across the top surface extending the width and length of the pool, but the fluid is cooler on its return path reducing the melt pool depth compared to a diffusion only driven system. The hydrodynamic mechanism is shown in figure 2*a* and the thermal field in figure 2*b*. The fluid flow and temperature field are typical of additive manufacturing and related welding processes [11] with flow velocities reaching up to $2\,\mathrm{m\,s^{-1}}$.

To validate these results, the melt pool dimensions were compared to X-ray radiography experimental results of Al10Si powder with a 100 W laser [5]. A good agreement was found with the experiments measuring a width of 120 μm, a length of 240 μm and a depth of 50 μm. This good match was only obtained when Marangoni flow was included in the model and an accurate representation of the thermal conditions of the powder was taken into consideration. Without fluid flow, either unrealistically high temperatures form at the spot or excessive energy is lost through evaporation. This result highlights the importance of resolving fluid flow in this process.

The microstructure results are given in figure 2*c,d*. Figure 2*c* shows the competitive nature between grains growing from the side and from the bottom of the melt pool, while figure 2*d*
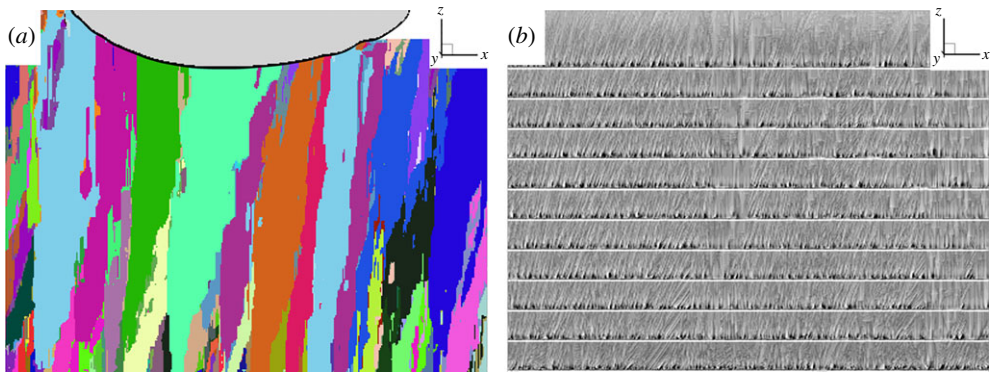
Figure 3. $\hat{\mathbf{B}} = 0$. (*a*) Grain structure and (*b*) concentration parallel to the scanning direction, image is taken behind the melt pool.

shows a cross-section of the fully formed solid behind the melt pool, where the microstructure can be inferred by variations in solute concentration with dark regions representing microsegregation. The melt pool boundary can be seen by the light coloured, low-concentration regions. In the centre just above the melt pool boundary, there is a higher solute concentration that can be attributed to solute transport from Marangoni flow. The convective rolls pass from the melt pool surface down along the solid/liquid interface and back to the centre. As flow passes along the interface, ejected solute from the solidifying side and rear of the melt pool is transported to the lower part of the melt pool where it is eventually captured by the solidification front. Figure 3*a*,*b* shows the grains and concentration in the cross-section parallel to the scanning direction. Figure 3*a* highlights the strong epitaxial growth which leads to the formation of very long grains in the build direction, these grains also tilt into the scanning direction as shown in the figure. Figure 3*b* shows the concentration, the white bands being low-concentration regions between successive layers. Figure 4 shows the experimental results from Singh *et al.* [52] where these key features are observed. The predicted features are quite typical of AM processing, and comparing figures 2*d* and 3*b* to figure 4, there is a qualitative agreement to experimental observations. The CA does provide some useful insight into the grain structure and distribution of concentration. In all the cases presented, the parallel cross-sections are quite similar, exhibiting tilted epitaxial growth, this is a consequence of scanning in exactly the same location with each layer. In practice, a more complex scanning strategy of hatching would normally be used with additional tracks on the side, as is the case of the experiments in figures 4*a*,*b*.

The strong thermal gradients inherent to this process can lead to substantial TE currents. The structure of these currents is shown in figure 5. High current flows in $+\hat{x}$ from the laser spot to the front of the melt pool then circulates through the solid/powder before re-entering upstream of the melt pool. The current density is lower as it re-enters the melt pool due to a much larger surface area than where it leaves, but the current occupies a much larger volume in $+\hat{z}$ as it returns to form the current loop near the spot. In general, the current in $\hat{y}$ is weak in the liquid compared to the other two components.

Current densities as high as 10^9 A m^{-2} are predicted; however, these high values are localized to the laser spot, with a volume average across the melt pool giving a lower value of 10^8 A m^{-2}. These results are consistent with the work of Kern *et al.* [35], who through estimation and direct measurement via the Hall effect found that currents in welding of steel could be as high as 14 A. Converting this to a current density over the characteristic length of their melt pool (300 µm) gives a current density of 10^8 A m^{-2}. With the thermal gradient orientated radially from the spot and referring to equation (2.1), $|\nabla \cdot \sigma S \nabla T| \gg 0$, therefore to satisfy $\nabla \cdot \mathbf{J} = 0$, the electric field balances over 85% of the TE field ($-\sigma S \nabla T$). Therefore, processing conditions directly linked to ∇T such as laser power and scan speed may have a significant effect on the magnitude of the resultant current density. Furthermore, as the laser spot can be close to the evaporation temperature, there
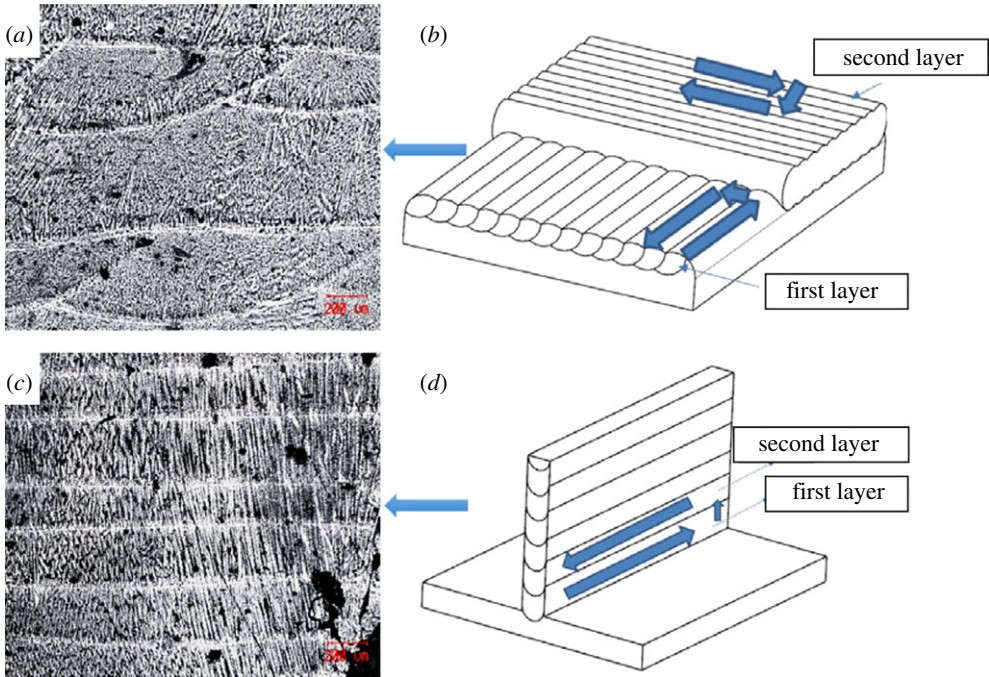
Figure 4. Experimental results from Singh *et al.* [52]. (*a*) Block sample optical micrograph, (*b*) block wall deposit scanning pattern, (*c*) single wall sample optical micrograph and (*d*) single wall deposit scanning pattern. Image reproduced under the Creative Commons Attribution Non-Commercial No Derivatives License from the Journal of Welding and Joining.
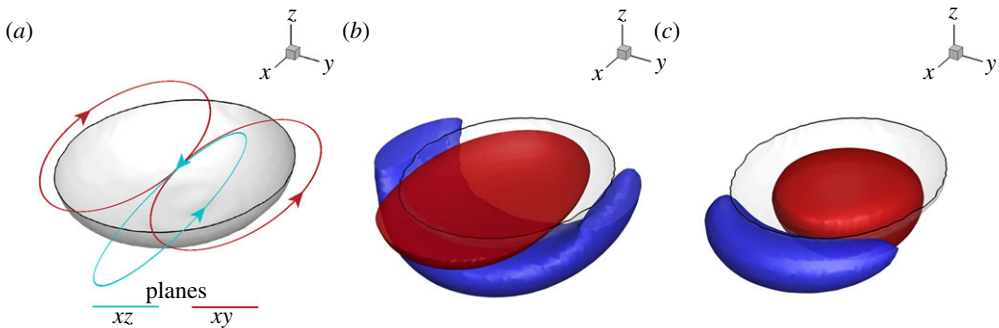

Figure 5. Current density **J**. (*a*) Schematic of dominant current circulations, (*b*) isosurfaces of $\pm 10^8$ A m^{-2}, positive (red) and negative (blue) J_x and (*c*) isosurfaces of $\pm 10^8$ A m^{-2}, positive (red) and negative (blue) J_z.

is a huge uncertainty in S, which is strongly dependent on temperature and phase. Taking the gross assumption that $\mathbf{E} = 0$ and therefore $\mathbf{J} \approx -\sigma S \nabla T$ to estimate the magnitude of S could yield results that are significantly lower.

(b) Case 2: keyhole-like effect and transition to thermoelectric magnetohydrodynamic flow, $\hat{\mathbf{B}} = -\hat{y}$

With an applied magnetic field orientated in $-\hat{y}$, the Lorentz force simplifies to $\mathbf{J} \times \mathbf{B} = (-J_z B_y)\hat{x} + (J_x B_y)\hat{z}$.
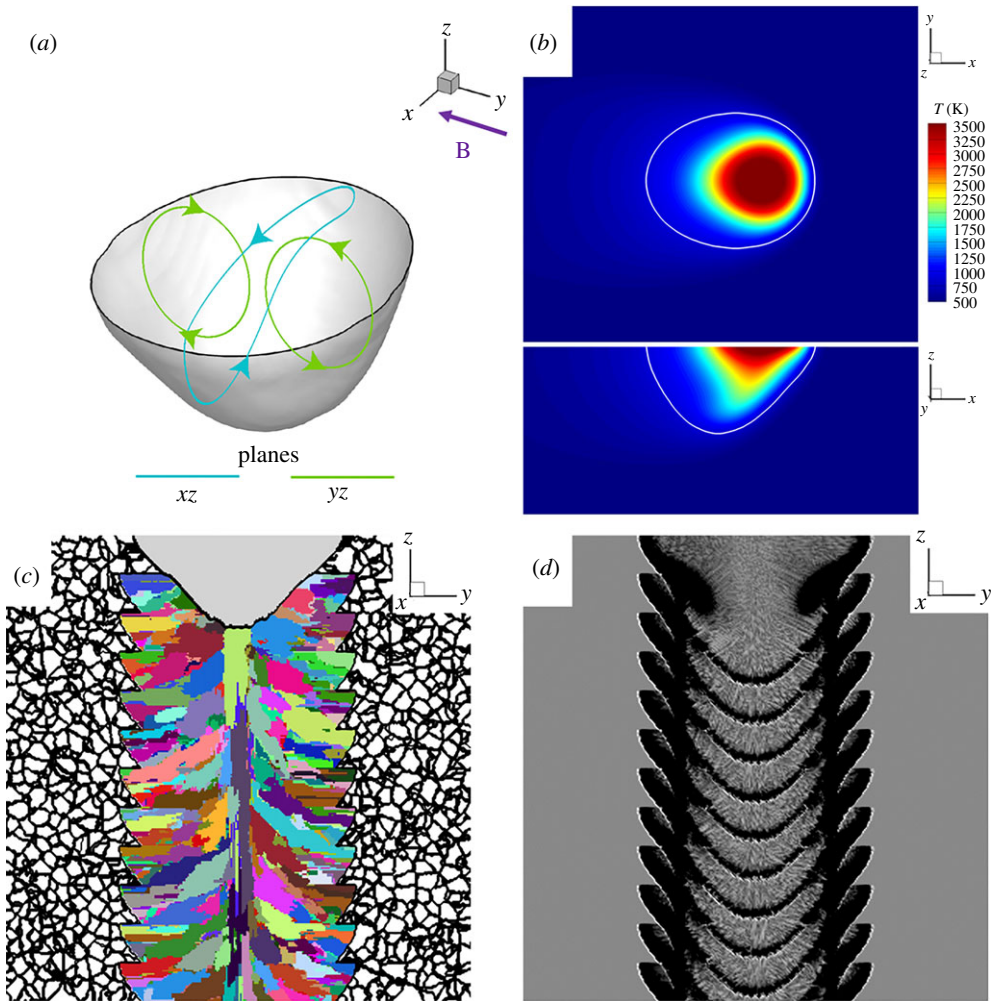
Figure 6. $\hat{\mathbf{B}} = -\hat{y}$. (a) Hydrodynamic mechanism. (b) Thermal field. Cross-section of microstructure perpendicular to scan direction. (c) Grain structure. (d) Solute concentration.

The force in $\hat{x}$ is generated by interacting with the larger volume current J_z and is directed towards the front of the melt pool. However, the main driver of this mechanism comes from the force in $\hat{z}$ which is localized to the laser spot and is orientated downward from the melt pool surface. This force competes directly with the returning Marangoni flow. When TEMHD is dominant, it has the effect of reversing the convective rolls, with flow downward from the spot and circulating back up the sides. Hot liquid near the spot is then transported down towards the base of the pool, melting deeper and creating a keyhole-like effect, with TEMHD velocities also reaching $2\,\mathrm{m\,s}^{-1}$. The force in $\hat{x}$ inadvertently reinforces this keyhole-like effect by transporting hot fluid towards the front of the melt pool, increasing the thermal gradient, which increases the TE currents and hence the force. Consequently, the melt becomes very deep but also narrow and short. Figure 6 shows the fluid mechanism, melt pool morphology and microstructure. Figure 6a highlights the TEMHD flow, with a single vortex along the centre and the side vortices in a reversed direction to Marangoni flow. The thermal profile in figure 6b shows the narrower and much deeper melt pool from the keyhole-like effect. On the microstructure side, figure 6c shows how hot fluid penetrating deep into the melt supresses the grains at the bottom and with a narrower melt pool and cooler fluid returning up the sides, the side grains are promoted to over grow the grains at the bottom. While this appears to suppress epitaxial growth, along
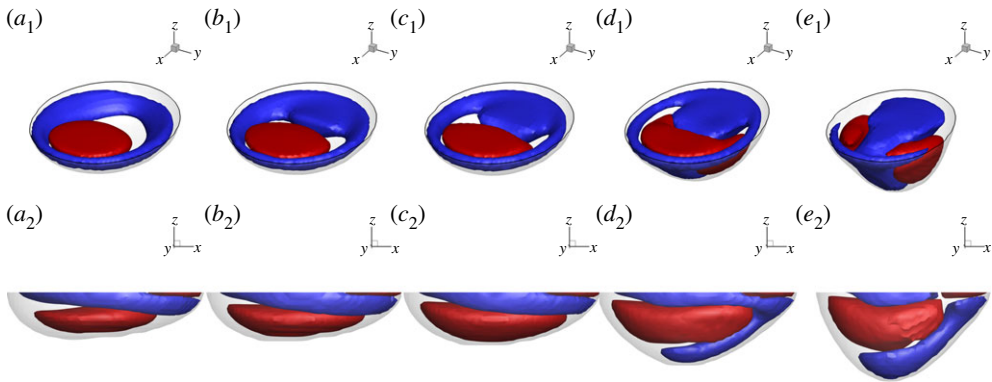
Figure 7. Transition from Marangoni flow to TEMHD flow with increasing magnetic field. (*a*) 0 T, (*b*) 0.15 T, (*c*) 0.3 T, (*d*) 0.4 T and (*e*) 0.5 T. Subscript 1 denotes isosurfaces for flow in $\hat{z}$, red is positive and blue negative. Subscript 2 denotes isosurfaces for flow in $\hat{x}$, red is positive and blue negative.

the centre line of the melt pool epitaxial growth is still essentially the same as that presented without a magnetic field in figure 3*a*. However, the grains are quite thin due to the competition with the side grains and their epitaxial growth is a consequence of scanning in the exact same position with each layer. Without perfect alignment to the centred grains, epitaxial growth could actually be disrupted. Figure 6*d* shows the solute concentration profile, where the dark regions of high concentration are a consequence of convective transport. The large-scale vortex in the *xz* plane also sweeps concentration from the solidifying base of the melt pool towards the back. Concentration builds up at the back of the melt pool and more gets captured into the solid.

In this case, the role of the critical field is also explored. By approximating $|\mathbf{J} \times \mathbf{B}| \approx |\mathbf{J}||\mathbf{B}|$, a simple force balance of $|\mathbf{J}||\mathbf{B}| = |(\partial\gamma/\partial T)\nabla T/L|$ can be used to estimate the strength of magnetic field required for TE forces to be comparable to Marangoni forces. However, as the Marangoni force is a surface force and the Lorentz force is a volume force, a characteristic length, L, is included. In this context, L should represent the length scale of fluid driven by the surface force, more specifically half of the length of the convective rolls of Marangoni flow. In Case 1, without a magnetic field, the upstream roll encompasses the entire depth of the melt pool and has a characteristic length of around $25\,\mu\text{m}$, while the downstream roll, which is confined to the front of the melt pool has a shorter length scale of $10\,\mu\text{m}$. Using these length scales, along with material properties and calculated values for $|\mathbf{J}|$ and $|\nabla T|$, the force balance yields critical fields at around 0.15 and 0.4 T. Figure 7 shows flows in $\hat{z}$ ($a_1 - e_1$) and in $\hat{x}$ ($a_2 - e_2$) for various magnetic field intensities ranging from 0 to 0.5 T. The figure shows the transition from purely Marangoni flow at 0 T (a_1 and a_2) to TEMHD dominated flow at 0.5 T (e_1 and e_2). The transition at 0.4 T is quite clear by comparing figure 7*c*–*e*, where the $\hat{z}$ component of the velocity reverses in the vicinity of the spot. The lower critical magnetic field is more subtle, but there is an indication of this when comparing figure 7*b*,*c*. The downward flow in $\hat{z}$ becomes closer to the spot with increasing magnetic field and the positive $\hat{x}$ flow at the lower surface of the melt pool is pushed past the laser spot. This indicates a stretching of the upstream vortex, where above this critical field, TEMHD begins to dominate and ultimately the vortex reaches the front of the melt pool. It then circulates to the back forming a single vortex. Based on this result, a magnetic field intensity of 0.5 T was chosen for all cases as TEMHD is just dominating over Marangoni flow.

(c) Case 3: extended melt pool, $\hat{B} = +\hat{y}$

In the presence of a magnetic field orientated in $+\hat{y}$, the Lorentz force becomes the same as Case 2; however, with the magnetic field reversed so too is the force. In $\hat{z}$, the force localized to the laser spot due to J_x is now orientated towards the surface of the melt pool. This is in the same direction
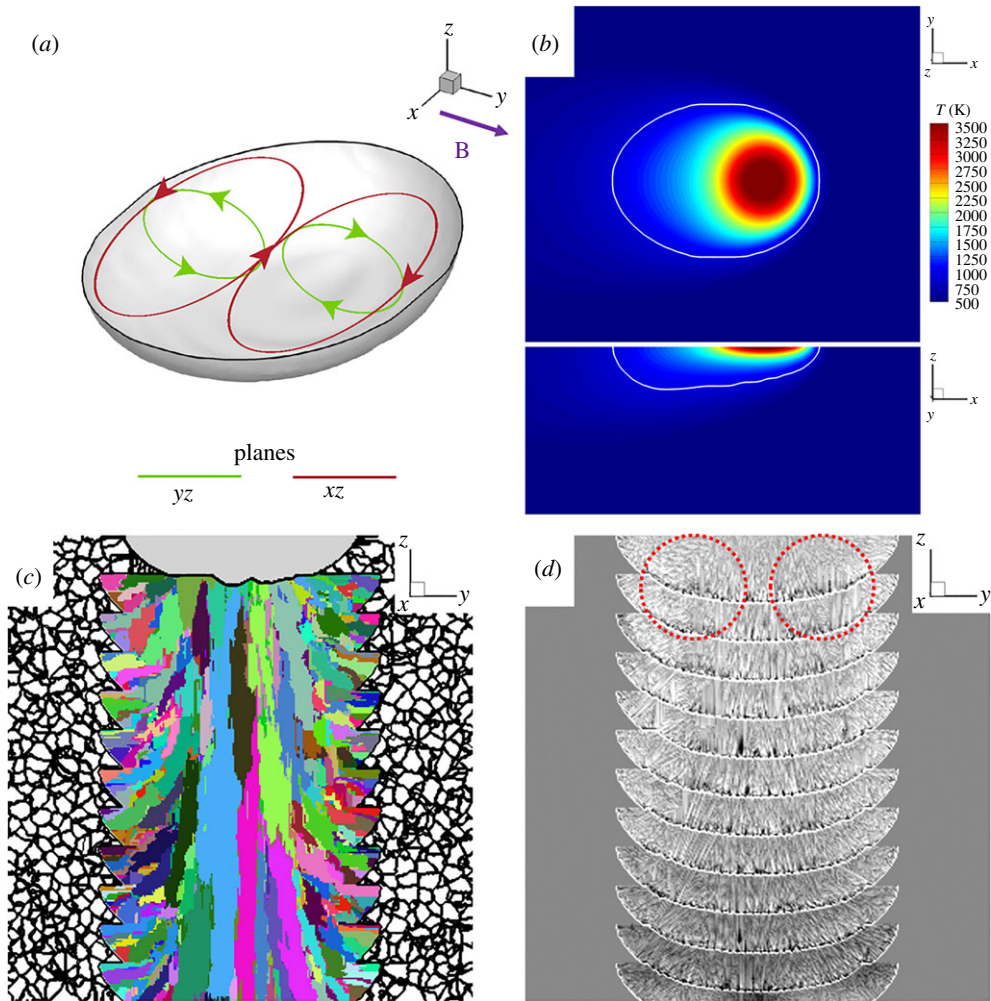
Figure 8. $\hat{\mathbf{B}} = +\hat{y}$. (*a*) Hydrodynamic mechanism. (*b*) Thermal field. Cross-section of microstructure perpendicular to scan direction. (*c*) Grain structure. (*d*) Concentration, the red circles highlighting regions of high concentration.

and location as the returning Marangoni flow and TEMHD acts to reinforce the Marangoni effect, causing the melt pool to become slightly wider and shallower. However, due to the shallowness of the melt pool, the dominant mechanism comes from the force in $\hat{x}$ generated by interacting with the larger volume current J_z and directed upstream. TEMHD overcomes Marangoni flow at the front of the melt pool, while promoting it upstream. This force pushes flow down the centre of the melt pool towards the back and recirculates along the sides generating a pair of vortices in the xy plane. Temperature is transported upstream, which has two effects. The first is that the melt pool becomes elongated and the second is that the thermal gradient at the front of the melt pool decreases. The latter reduces the TE effect and so TEMHD is weaker; however, since both the Marangoni force and TE force are dependent on the thermal gradient, TEMHD is still dominant. These effects are highlighted in figure 8, where the fluid flow mechanisms are shown in figure 8*a* and temperature in figure 8*b*. An important effect that cannot be yet captured by the current model is the change in the free surface of the melt pool. With a force at the surface pointing upwards, this could amplify the 'balling' observed in experiments. Observations from a transverse field in welding have shown that depending on the orientation balling can be enhanced or supressed [35]. Although it cannot be directly predicted here, the direction and relative strength of the TE force

is consistent with these findings. Without a free surface, the melt pool is constrained and so in reality, the influence of the magnetic field in this case could be much larger than predicted.

Figure 8*c* shows the grain structure; where there is still a strong epitaxial growth along the centre similar to Case 1 with $\mathbf{B} = 0$. TEMHD may also further promote epitaxial growth with increased flow of hot fluid to the sides of the melt pool, suppressing the growth of side grains, while conversely cooler fluid returning to the spot allowing the bottom grains to grow first. However, in this case, the relatively poor heat transfer between the side of the melt pool and the powder reduces this effect, but in more complex scanning strategies where the sides of the melt pool would be in contact with solid rather than powder, this effect would be amplified. Figure 8*d* shows the solute concentration distribution. The variations are quite low, but there are two high-concentration regions either side of the centre line highlighted in the figure. This can be attributed to the twin circulations in the xy plane, where at the back of the melt pool, a stagnation point exists at the solid–liquid interface and flow points $\pm\hat{y}$ either side of this. High concentration is transported away from the centre forming these two regions.

(d) Case 4: deflected melt pool, $\hat{B} = +\hat{z}$

This case investigates a magnetic field orientated in the direction of build. Owing to the symmetry of the problem set-up, it is only necessary to consider one orientation, namely $+\hat{z}$, as the opposite direction leads to a mirror image along the yz plane. The Lorentz force in this case becomes $\mathbf{J} \times \mathbf{B} = (J_y B_z)\hat{x} - (J_x B_z)\hat{y}$ where the main interaction is with the highly localized J_x current. This creates a strong force at the top surface and at the front of the melt pool in $-\hat{y}$ that introduces two vortices. The first is circulating around the top of the melt pool in the xy plane and the second is along the front of the melt pool in the xz plane. Both have a strong velocity $(2\,\mathrm{m\,s}^{-1})$ in $-\hat{y}$ at the front of the melt pool that transports hot fluid tangentially to the scan direction, causing the melt pool to deflect and become asymmetric. As cooler fluid returns on the $+\hat{y}$ side of the melt pool, isotherms become condensed in this region. This increases the tangential thermal gradient between the spot and the edge of the melt pool in $+\hat{y}$; consequently, the TE currents twist exiting the melt pool with a relatively high component in $+\hat{y}$ as well as $+\hat{x}$. This stronger J_y component of the current density then interacts with the magnetic field giving a force in $+\hat{x}$ at the top surface. In addition to the Marangoni force, this generates convective rolls at the front of the melt pool, that when combined with the other larger scale circulations turn into a swirl flow along the front of the melt pool. These fluid mechanisms are highlighted in figure 9*a* along with the drastic change in melt pool morphology and thermal profile in figure 9*b*. Owing to the deflection, the effective melt pool width is much wider than in the previous cases. This can be seen in the microstructure results given in figure 9*c* where the bottom grains grow off-centre, while the beam is still in the centre of the figure. This still creates epitaxial growth, but now at the tail edge of the deflected melt pool. Figure 9*d* shows the solute concentration, where there is a clear band of high concentration across the melt pool. This can be attributed to the large-scale circulation in the xy plane, where solute begins to be transported from the $-\hat{y}$ side of the melt pool and sweeping across the entire solid–liquid interface at the rear of the melt pool. This large length scale of transport causes high concentrations to build up at the back of the melt pool and ultimately get captured in the microstructure.

(e) Case 5: magnetic field along the scan direction, $\hat{B} = +\hat{x}$

The final case looks at the magnetic field aligned with the scanning direction and again due to symmetry of the problem only the $+\hat{x}$ magnetic field is considered, as the negative would be mirrored along the xz plane. The Lorentz force becomes $\mathbf{J} \times \mathbf{B} = (J_z B_x)\hat{y} - (J_y B_x)\hat{z}$, where in contrast with all the previous magnetic field cases, there is no interaction with the high and localized J_x current. Here, the main driver for the fluid mechanism comes from the lower intensity, but higher volume current density in $\hat{z}$ acting across large sections of the melt pool. Owing to the large volume of liquid J_z occupies, the resulting force acts to push a large column of fluid
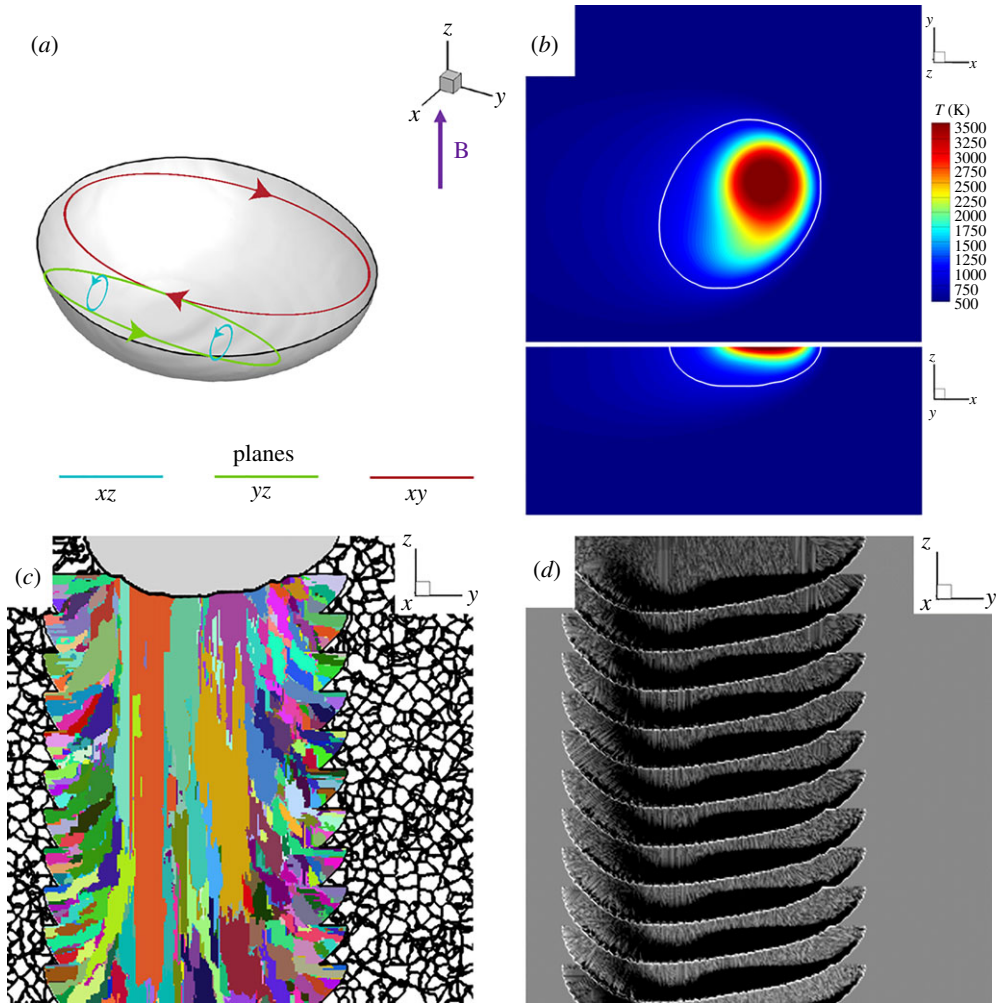
Figure 9. $\hat{\mathbf{B}} = +\hat{z}$. (*a*) Hydrodynamic mechanism. (*b*) Thermal field. Cross-section of microstructure perpendicular to scan direction. (*c*) Grain structure. (*d*) Concentration.

extending from the bottom of the melt pool all the way to the top near the spot in $+\hat{y}$ direction. With the force extending throughout the depth of the melt pool, the fluid is unable to form circulations in the yz plane and instead forms a pair of counter-rotating vortices in the xz plane, one ahead of the spot and one upstream. There is no TE force parallel to the magnetic field in $\hat{x}$, but due to the large thermal gradients at the front of the melt pool, the Marangoni force is still pushing flow downstream. The Marangoni flow introduces a convective roll in the xz plane which causes the TEMHD flow to circulate back at the bottom of the melt pool. Upstream this effect is less prevalent due to the lower thermal gradients. However, J_z does increase slightly as it approaches the spot; therefore, the counter-rotating vortices try to form at the top surface. Owing to Marangoni flow, which is stronger at the front of the melt pool, these counter-rotating vortices are not quite in the yz plane instead rotating at a tilted angle, where the downstream end returns along the base of the melt pool while the upstream end predominantly returns across the top surface. Although the fluid mechanisms are complex, the effect on the melt pool is relatively weak compared to the previous cases. This can be attributed to lack of interaction with the dominant J_x component and the magnetic field, but also because thermal transport is relatively localized with no large-scale circulations. However, there is a slight deflection of the melt pool.
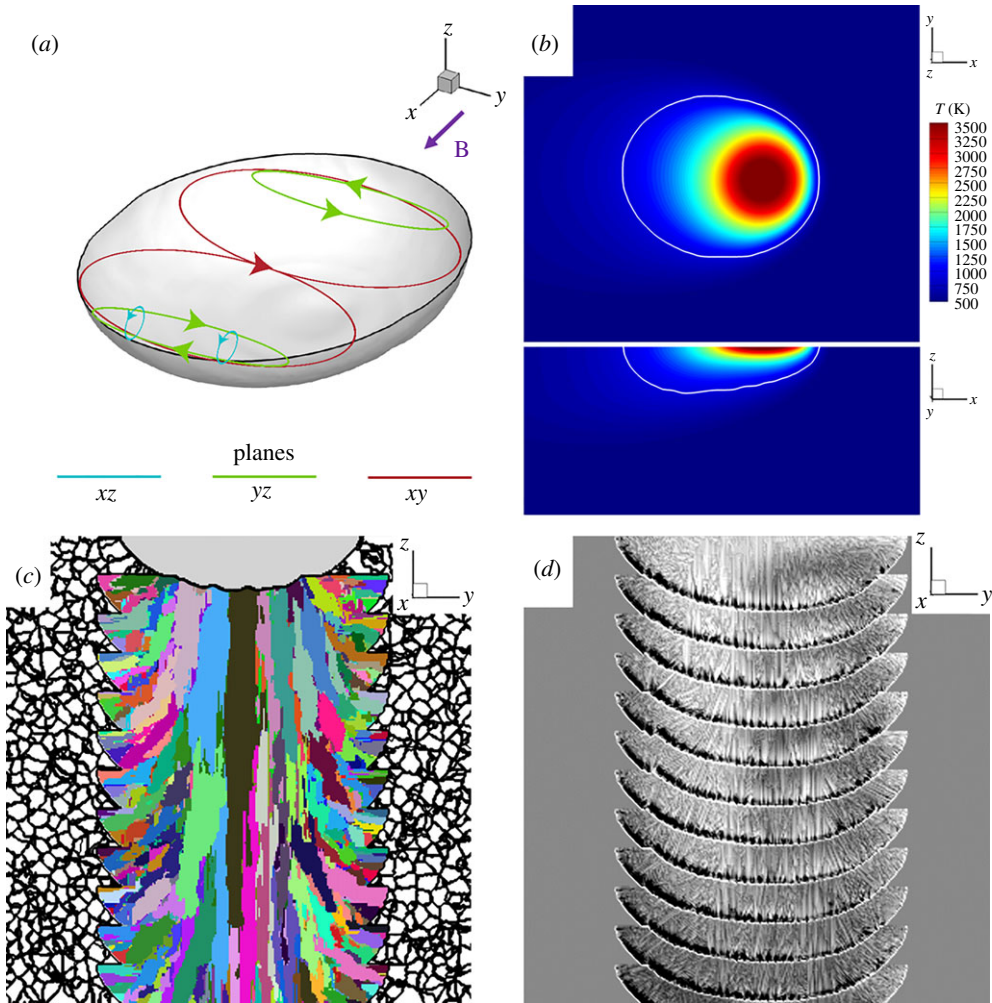
Figure 10. $\hat{\mathbf{B}} = +\hat{x}$. (a) Hydrodynamic mechanism. (b) Thermal field. Cross-section of microstructure perpendicular to scan direction. (c) Grain structure. (d) Concentration.

Figure 10a shows the fluid mechanisms and figure 10b shows the thermal field. Owing to the weaker thermal transport introduced by TEMHD compared to other cases, the microstructure here exhibits essentially similar features to Case 1 where there is no magnetic field. A cross-section of the grain structure is given in figure 10c and exhibits very similar structures to Case 1. However, the concentration distribution is quite different as shown in figure 10d. High concentration builds up in the lower $-\hat{y}$ corner due to the circulation in the yz plane transporting concentration from the side wall down to the bottom. The circulation in the xy plane transports high concentration from the $+\hat{y}$ resulting in the dark bands on the right-hand side of the melt pool in figure 10d.

4. Conclusion

By using a combined LBM for fluid flow and an enthalpy-based method for solidification during the additive manufacturing process, mesoscopic calculations of the melt dynamics were predicted that are in good agreement with experiments from the literature. Then, by also resolving the TE currents arising from Seebeck discontinuities at the solid–liquid interface, their interaction with an

externally applied magnetic field was examined. A parametric study of magnetic field orientation and strength on melt pool dynamics revealed the transition from Marangoni flow to TEMHD flow. Convective heat transport modified the melt pool shape and thermal distributions. Steady-state solutions were presented for each orthogonal magnetic field orientation, revealing key hydrodynamic mechanisms. Noteworthy results were the formation of a keyhole-like mechanism and deflection of the melt pool. Taking these steady-state solutions in combination with a CA-based grain growth model, the microstructure evolution over multiple layers was captured. The results indicated that the grain morphology can be modified by the application of a magnetic field and therefore potentially controlled. Analysis of the concentration in the context of the predicted hydrodynamics mechanisms showed that TEMHD may also be used to control solute distribution. There are many key assumptions taken in this work that could have a strong impact or interaction with TEMHD including free surface and the change to thermal transport over successive layers of solid. Further work is necessary to increase accuracy, and this could include transient and two-way coupling, determining the optimal value for the partition coefficient in CA, but also the addition of key phenomena that influence or interact with TEMHD, such as a free surface. However, despite these simplifications, this work shows good qualitative comparisons against available experimental evidence and provides an initial theoretical basis of how magnetic fields can be used to control melt pool dynamics and microstructure in AM processes.

References

1. Acharya R, Sharon JA, Staroselsky A. 2017 Prediction of microstructure in laser powder bed fusion process. *Acta Mater.* **124**, 360–371. (doi:10.1016/j.actamat.2016.11.018)
2. King WE, Anderson AT, Ferencz R, Hodge N, Kamath C, Khairallah SA, Rubenchik AM. 2015 Laser powder bed fusion additive manufacturing of metals; physics, computational, and materials challenges. *Appl. Phys. Rev.* **2**, 041304. (doi:10.1063/1.4937809)
3. Körner C, Attar E, Heinl P. 2011 Mesoscopic simulation of selective beam melting processes. *J. Mater. Process. Technol.* **211**, 978–987. (doi:10.1016/j.jmatprotec.2010.12.016)
4. Shifeng W, Shuai L, Qingsong W, Yan C, Sheng Z, Yusheng S. 2014 Effect of molten pool boundaries on the mechanical properties of selective laser melting parts. *J. Mater. Process. Technol.* **214**, 2660–2667. (doi:10.1016/j.jmatprotec.2014.06.002)
5. Guo Q *et al.* 2019 In-situ characterization and quantification of melt pool variation under constant input energy density in laser powder-bed fusion additive manufacturing process. *Addit. Manuf.* **28**, 600–609. (doi:10.1016/j.addma.2019.04.021)
6. Thompson SM, Bian L, Shamsaei N, Yadollahi A. 2015 An overview of direct laser deposition for additive manufacturing; part I: transport phenomena, modeling and diagnostics. *Addit. Manuf.* **8**, 36–62. (doi:10.1016/j.addma.2015.07.001)
7. Shamsaei N, Yadollahi A, Bian L, Thompson SM. 2015 An overview of direct laser deposition for additive manufacturing; part II: mechanical behavior, process parameter optimization and control. *Addit. Manuf.* **8**, 12–35. (doi:10.1016/j.addma.2015.07.002)
8. Gusarov A, Yadroitsev I, Bertrand P, Smurov I. 2009 Model of radiation and heat transfer in laser-powder interaction zone at selective laser melting. *J. Heat Transfer* **131**, 072101. (doi:10.1115/1.3109245)

9. Geiger M, Leitz KH, Koch H, Otto A. 2009 A 3D transient model of keyhole and melt pool dynamics in laser beam welding applied to the joining of zinc coated sheets. *Prod. Eng.* **3**, 127–136. (doi:10.1007/s11740-008-0148-7)

10. Yuan P, Gu D. 2015 Molten pool behaviour and its physical mechanism during selective laser melting of TiC/AlSi10 Mg nanocomposites: simulation and experiments. *J. Phys. D: Appl. Phys.* **48**, 035303. (doi:10.1088/00223727/48/3/035303)

11. Khairallah SA, Anderson AT, Rubenchik A, King WE. 2016 Laser powderbed fusion additive manufacturing: physics of complex melt flow and formation mechanisms of pores, spatter, and denudation zones. *Acta Mater.* **108**, 36–45. (doi:10.1016/j.actamat.2016.02.014)

12. Matthews MJ, Guss G, Khairallah SA, Rubenchik AM, Depond PJ, King WE. 2016 Denudation of metal powder layers in laser powder bed fusion processes. *Acta Mater.* **114**, 33–42. (doi:10.1016/j.actamat.2016.05.017)

13. Hodge NE, Ferencz RM, Solberg JM. 2014 Implementation of a thermomechanical model for the simulation of selective laser melting. *Comput. Mech.* **54**, 33–51. (doi:10.1007/s00466-014-1024-2)

14. Morville S, Carin M, Peyre P, Gharbi M, Carron D, Masson PL, Fabbro R. 2012 2D longitudinal modeling of heat transfer and fluid flow during multilayered direct laser metal deposition process. *J. Laser Appl.* **24**, 032008. (doi:10.2351/1.4726445)

15. Wang X, Chou K. 2018 Microstructure simulations of Inconel 718 during selective laser melting using a phase field model. *Int. J. Adv. Manuf. Tech.* **100**, 2147–2162. (doi:10.1007/s00170-018-2814-z)

16. Radhakrishnan B, Gorti SB, Turner JA, Acharya R, Sharon JA, Staroselsky A, El-Wardany T. 2018 Phase field simulations of microstructure evolution in IN718 using a surrogate Ni–Fe–Nb alloy during laser powder bed fusion. *Metals* **9**, 14. (doi:10.3390/met9010014)

17. Loh LE, Chua CK, Yeong WY, Song J, Mapar M, Sing SL, Liu ZH, Zhang DQ. 2015 Numerical investigation and an effective modelling on the selective laser melting (SLM) process with aluminium alloy 6061. *Int. J. Heat Mass Transfer* **80**, 288–300. (doi:10.1016/j.ijheatmasstransfer.2014.09.014)

18. Gürtler FJ, Karg M, Leitz KH, Schmidt M. 2013 Simulation of laser beam melting of steel powders using the three-dimensional volume of fluid method. *Phys. Procedia* **41**, 881–886. (doi:10.1016/j.phpro.2013.03.162)

19. Lian Y, Gan Z, Yu C, Kats D, Liu WK, Wagner GJ. 2019 A cellular automaton finite volume method for microstructure evolution during additive manufacturing. *Mater. Des.* **169**, 107672. (doi:10.1016/j.matdes.2019.107672)

20. Koepf JA, Gotterbarm MR, Markl M, Körner C. 2018 3D multi-layer grain structure simulation of powder bed fusion additive manufacturing. *Acta Mater.* **152**, 119–126. (doi:10.1016/j.actamat.2018.04.030)

21. Rai A, Markl M, Körner C. 2016 A coupled cellular automaton–lattice Boltzmann model for grain structure simulation during additive manufacturing. *Comput. Mat. Sci.* **124**, 37–48. (doi:10.1016/j.commatsci.2016.07.005)

22. Ibrahim KA, Wu B, Brandon NP. 2016 Electrical conductivity and porosity in stainless steel 316 L scaffolds for electrochemical devices fabricated using selective laser sintering. *Mater. Des.* **106**, 51–59. (doi:10.1016/j.matdes.2016.05.096)

23. Singh R, Lee PD, Dashwood RJ, Lindley TC. 2010 Titanium foams for biomedical applications: a review. *Mater. Technol.* **25**, 127–136. (doi:10.1179/175355510×12744412709403)

24. Murr LE. 2016 Frontiers of 3D printing/additive manufacturing: from human organs to aircraft fabrication. *J. Mater. Sci. Technol.* **32**, 987–995. (doi:10.1016/j.jmst.2016.08.011)

25. Zhang B, Li Y, Bai Q. 2017 Defect formation mechanisms in selective laser melting: a review. *Chin. J. Mech. Eng.* **30**, 515–527. (doi:10.1007/s10033-017-0121-5)

26. Leung CLA, Marussi S, Atwood RC, Towrie M, Withers PJ, Lee PD. 2018 In situ x-ray imaging of defect and molten pool dynamics in laser additive manufacturing. *Nat. Commun.* **9**, 1–9. (doi:10.1038/s41467-018-03734-7)

27. Li R, Shi Y, Wang Z, Wang L, Liu J, Jiang W. 2010 Densification behavior of gas and water atomized 316 L stainless steel powder during selective laser melting. *Appl. Surf. Sci.* **256**, 4350–4356. (doi:10.1016/j.apsusc.2010.02.030)

28. Fautrelle Y, Wang J, Salloum-Abou-Jaoude G, Abou-Khalil L, Reinhart G, Li X, Ren ZM, Nguyen-Thi H. 2018 Thermo-electric-magnetic hydrodynamics in solidification: in situ observations and theory. *JOM* **70**, 764–771. (doi:10.1007/s11837-018-2777-4)

29. Kao A, Cai B, Lee P, Pericleous K. 2017 The effects of thermoelectric magnetohydrodynamics in directional solidification under a transverse magnetic field. *J. Cryst. Growth* **457**, 270–274. (doi:10.1016/j.jcrysgro.2016.07.003)

30. Kaldre I, Fautrelle Y, Etay J, Bojarevics A, Buligins L. 2013 Thermoelectric current and magnetic field interaction influence on the structure of directionally solidified Sn–10 wt.%Pb alloy. *J. Alloys Compd.* **571**, 50–55. (doi:10.1016/j.jallcom.2013.03.211)

31. Gao J, Han M, Kao A, Pericleous K, Alexandrov DV, Galenko PK. 2016 Dendritic growth velocities in an undercooled melt of pure nickel under static magnetic fields: a test of theory with convection. *Acta Mater.* **103**, 184–191. (doi:10.1016/j.actamat.2015.10.014)

32. Kao A, Gao J, Pericleous K. 2018 Thermoelectric magnetohydrodynamic effects on the crystal growth rate of undercooled Ni dendrites. *Phil. Trans. R. Soc. A* **376**, 20170206. (doi:10.1098/rsta.2017.0206)

33. Du D, Haley JC, Dong A, Fautrelle Y, Shu D, Zhu G, Li X, Sun B, Lavernia EJ. 2019 Influence of static magnetic field on microstructure and mechanical behavior of selective laser melted AlSi10 Mg alloy. *Mater. Des.* **181**, 107923. (doi:10.1016/j.matdes.2019.107923)

34. Chen J, Wei Y, Zhan X, Pan P. 2017 Weld profile, microstructure, and mechanical property of laser-welded butt joints of 5A06 Al alloy with static magnetic field support. *Int. J. Adv. Manuf. Tech.* **92**, 1677–1686. (doi:10.1007/s00170-017-0268-3)

35. Kern M, Berger P, Hugel H. 2000 Magneto-fluid dynamic control of seam quality in CO_2 laser beam welding. *Weld. J. Res. Suppl.* **79**, 72s.

36. Shercliff JA. 1979 Thermoelectric magnetohydrodynamics. *J. Fluid Mech.* **91**, 231–251. (doi:10.1017/s0022112079000136)

37. Kao A, Krastins I, Alexandrakis M, Shevchenko N, Eckert S, Pericleous K. 2018 A parallel cellular automata lattice Boltzmann method for convection-driven solidification. *JOM* **71**, 48–58. (doi:10.1007/s11837-0183195-3)

38. Kao A, Shevchenko N, Alexandrakis M, Krastins I, Eckert S, Pericleous K. 2019 Thermal dependence of large-scale freckle defect formation. *Phil. Trans. R. Soc. A* **377**, 20180206. (doi:10.1098/rsta.2018.0206)

39. Voller VR, Cross M, Markatos NC. 1987 An enthalpy method for convection/diffusion phase change. *Int. J. Numer. Methods Eng.* **24**, 271–284. (doi:10.1002/nme.1620240119)

40. Qiu C, Panwisawas C, Ward M, Basoalto HC, Brooks JW, Attallah MM. 2015 On the role of melt flow into the surface structure and porosity development during selective laser melting. *Acta Mater.* **96**, 72–79. (doi:10.1016/j.actamat.2015.06.004)

41. Hughes M, Taylor GA, Pericleous K. 2000 Thermocapillary and magnetohydrodynamic effects in modelling the thermodynamics of stationary welding processes. *Phoenics J. Comput. Fluid Dyn. Appl.* **13**, 99–113.

42. Zhang S, Lane B, Whiting J, Chou K. 2019 On thermal properties of metallic powder in laser powder bed fusion additive manufacturing. *J. Manuf. Processes* **47**, 382–392. (doi:10.1016/j.jmapro.2019.09.012)

43. Wang W, Lee P, McLean M. 2003 A model of solidification microstructures in nickel-based superalloys: predicting primary dendrite spacing selection. *Acta Mater.* **51**, 2971–2987. (doi:10.1016/s1359-6454(03)00110-1)

44. Yuan L, Lee PD. 2010 Dendritic solidification under natural and forced convection in binary alloys: 2D versus 3D simulation. *Modell. Simul. Mater. Sci. Eng.* **18**, 055008. (doi:10.1088/0965-0393/18/5/055008)

45. Yuan L, Lee PD. 2012 A new mechanism for freckle initiation based on microstructural level simulation. *Acta Mater.* **60**, 4917–4926. (doi:10.1016/j.actamat.2012.04.043)

46. Aziz MJ, Kaplan T. 1988 Continuous growth model for interface motion during alloy solidification. *Acta Metall.* **36**, 2335–2347. (doi:10.1016/00016160(88)90333-1)

47. Liu X, Zhao C, Zhou X, Shen Z, Liu W. 2019 Microstructure of selective laser melted AlSi10 Mg alloy. *Mater. Des.* **168**, 107677. (doi:10.1016/j.matdes.2019.107677)

48. Overfelt R, Bakhtiyarov S, Taylor R. 2002 Thermophysical properties of A201, A319, and A356 aluminium casting alloys. *High Temp. High Press.* **34**, 401–409. (doi:10.1068/htjr052)

49. Soylemez E, Koç E, Coşkun M. 2019 Thermo-mechanical simulations of selective laser melting for AlSi10 Mg alloy to predict the part-scale deformations. *Prog. Addit. Manuf.* **4**, 465–478. (doi:10.1007/s40964-019-00096-4)

50. Leitner M, Leitner T, Schmon A, Aziz K, Pottlacher G. 2017 Thermophysical properties of liquid aluminum. *Met. Trans. A* **48**, 3036–3045. (doi:10.1007/s11661-017-4053-6)

51. Lan Q, Cheng C, Zhang J, Guo R, Le Q. 2019 The relationship between the thermoelectric power and resultant solidification microstructures of AlSi melt under electromagnetic field. *Mater. Chem. Phys.* **231**, 203–215. (doi:10.1016/j.matchemphys.2019.04.021)
52. Singh A, Ramakrishnan A, Dinda G. 2017 Fabrication of Al-11.2Si components by direct laser metal deposition for automotive applications. *J. Weld. Join.* **35**, 67–73. (doi:10.5781/jwj.2017.35.4.10)

20

royalsocietypublishing.org/journal/rsta *Phil. Trans. R. Soc. A* **378**: 20190249